Probabilistic economic seismic loss estimation in steel buildings using post-tensioned moment-resisting frames and viscous dampers

Athanasios I. Dimopoulos[1], Angelos S. Tzimas[1], Theodore L. Karavasilis[1,*], Dimitrios Vamvatsikos[2]

[1]*School of Engineering, University of Warwick, CV4 7AL Coventry, United Kingdom*
[2]*National Technical University of Athens, 15780 Athens, Greece*

SUMMARY

The potential of post-tensioned self-centering moment-resisting frames (SC-MRFs) and viscous dampers to reduce the economic seismic losses in steel buildings is evaluated. The evaluation is based on a prototype steel building designed using four different seismic-resistant frames: (a) conventional moment resisting frames (MRFs); (b) MRFs with viscous dampers; (c) SC-MRFs; or (d) SC-MRFs with viscous dampers. All frames are designed according to Eurocode 8, and have the same column/beam cross-sections and similar periods of vibration. Viscous dampers are designed to reduce the peak story drift under the design basis earthquake (DBE) from 1.8% to 1.2%. Losses are estimated by developing vulnerability functions according to the FEMA P-58 methodology, which considers uncertainties in earthquake ground motion, structural response, and repair costs. Both the probability of collapse and the probability of demolition due to excessive residual story drifts are taken into account. Incremental dynamic analyses are conducted using models capable to simulate all limit states up to collapse. A parametric study on the effect of the residual story drift threshold beyond which is less expensive to rebuild a structure than to repair is also conducted. It is shown that viscous dampers are more effective than post-tensioning for seismic intensities equal or lower than the maximum considered earthquake (MCE). Post-tensioning is effective in reducing repair costs only for seismic intensities higher than the DBE. The paper also highlights the effectiveness of combining post-tensioning and supplemental viscous damping by showing that the SC-MRF with viscous dampers achieves significant repair cost reductions compared to the conventional MRF.

KEY WORDS: Steel frames; self-centering; viscous dampers; loss estimation; collapse; residual drifts; Eurocode 8

[*]Corresponding Author. Tel.: +44 (0)2476522363. *E-mail address:* T.Karavasilis@warwick.ac.uk
Engineering and Physical Sciences Research Council of the United Kingdom; Grant Ref: EP/K006118/1

1. INTRODUCTION

The February 2011 Christchurch earthquake confirmed that conventional seismic-resistant structures, such as steel moment-resisting frames (MRFs), experience difficult-to-repair damage due to large story drifts, residual story drifts, and inelastic deformations in structural members. After that earthquake, a significant percentage of the buildings were declared unusable, while the reconstruction cost was estimated approximately equal to 40 billion NZ dollars [1-2]. These socio-economic losses highlight the need to use in practice more resilient structural systems that are less vulnerable and easier to repair after strong earthquakes.

Steel self-centering moment-resisting frames (SC-MRFs) with post-tensioned (PT) beam-column connections are a class of resilient seismic-resistant structures that eliminate beam inelastic deformations and residual story drifts [3-13]. Practical performance-based seismic design procedures for SC-MRFs are proposed in [14-15]. Another class of resilient structures are steel MRFs with passive dampers, which reduce story drifts, and indirectly, inelastic deformations and residual story drifts [16-19].

The combination of self-centering systems with passive dampers has been explored in few research studies. Using viscous dampers in parallel to self-centering precast concrete base rocking walls was proposed as an effective way to simultaneously control peak story drifts and residual story drifts [20]. The parallel combination of hysteretic and viscous energy dissipation, along with a friction slip mechanism in series connected to the viscous energy dissipation mechanism, were found to improve the seismic performance of self-centering systems [21]. A recent study shows that the combination of viscous dampers and steel SC-MRFs leads to simultaneous control of inelastic deformations, peak story drifts, and residual story drifts [22].

To properly assess the seismic resilience of a structural system, the actual economic seismic losses should be rigorously estimated. This can be accomplished using procedures that quantify and propagate uncertainties such as the early one developed by Porter et al. [23], which uses nonlinear dynamic analyses, predicts damage at the component level using fragility functions, and finally estimates the total building repair cost. This procedure was further developed to become the PEER (Pacific Earthquake Engineering Research) methodology that is now known as the 2nd generation performance based earthquake engineering (PBEE-2) [24]. Early studies on PBEE-2 showed that component damageability and ground motion time histories have strong influence on loss uncertainty, while material properties and other uncertainties in the structural model may have relatively little influence [25-26]. Ramirez and Miranda [27] showed how the probability of having to demolish a building as the result of excessive residual story drifts influences seismic loss estimation. Furthermore, they conducted sensitivity analysis to show that the estimate of loss is more sensitive to the median residual drift threshold for demolition rather than its dispersion. A critical review of PBEE-2 and examination of its limitations has been conducted by Gunay and Mosalam [28]. The state-of-art in economic seismic loss estimation is described by the FEMA P-58 methodology that adopts PBEE-2 along with a database of structural and non-structural component fragility functions and repair cost estimates [29].

The literature review shows that the potential of steel SC-MRFs with viscous dampers to reduce economic seismic losses by simultaneously controlling structural and non-structural damage has not been assessed and quantified. This quantification is of particular interest to justify the design complexity in combining the post-tensioning and passive energy dissipation technologies. To properly evaluate and compare the economic seismic losses of steel buildings using either SC-MRFs with viscous dampers or conventional MRFs, a parametric study on the effect of the assumed residual story drift value beyond which is less expensive to

rebuild a structure than to repair should be conducted. Moreover, the effect of the probability of collapse due to dynamic instability should be considered.

In an attempt to partially address such issues, a prototype steel building is designed using four different lateral load-resisting systems, i.e. conventional MRF and SC-MRF both with and without viscous dampers. To achieve a fair comparison, design was performed for all cases according to Eurocode 8, using the same member dimensions and having similar periods of vibration. The results shed light on the potential of PT connections and supplemental viscous damping to reduce repair costs under different definitions of the demolition criterion and highlights the superior performance achieved when these two technologies are combined. Seismic performance is compared at the level of vulnerability, i.e. seismic loss given the seismic intensity. A more definite evaluation and comparison would require completing the analysis by considering the seismic hazard at different potential sites.

2. SC-MRFs USING PT CONNECTIONS WITH WHPs

Figure 1(a) shows a SC-MRF using PT connections with web hourglass shape pins (WHPs) and Figure 1(b) shows an exterior PT connection with WHPs. This connection has been experimentally and numerically evaluated by Vasdravellis et al. [7-8]. Two high strength steel bars located at the mid depth of the beam, one at each side of the beam web, pass through holes drilled on the column flanges. The bars are post-tensioned and anchored to the exterior columns. WHPs are inserted in aligned holes on the beam web and on supporting plates welded to the column flanges. Energy is dissipated through inelastic bending of the WHPs that have an optimized hourglass shape (Figure 1(c)) with enhanced fracture capacity [30]. The beam web and flanges are reinforced with steel plates. The panel zone is strengthened with doubler and continuity plates. A fin plate welded on the column flange and bolted on the beam web is used for easy erection and resistance against gravity loads before post-tensioning. Slotted holes on the beam web ensure negligible influence of the fin plate on the PT connection hysteretic behavior.

The connection behavior is characterized by gap opening and closing in the beam-column interface and re-centering capability as the result of the force in the PT bars. A discontinuous steel-concrete composite slab is used to avoid damage in the slab as the gaps in the PT connections open and close [22]. Figure 2(a) shows the free body diagram of an external PT connection where d_{1u} and d_{1l} are the distances of the upper and lower WHPs from the center of rotation that is assumed to be at the inner edge of the beam flange reinforcing plates; d_2 is the distance of the PT bars from the center of rotation; T is the total force in both PT bars; $F_{WHP,u}$ and $F_{WHP,l}$ are the forces in the upper and lower WHPs; C_F is the compressive force in the beam-column interface; V_{C1u} and V_{C1l} are the shear forces in the upper and lower column, M is the PT connection moment, V is the beam shear force; and N is the horizontal clamping force that is transferred to the beam-column interface through the slab diaphragm and the beam. Figure 2(b) shows the SC-MRF expansion due to rotations θ in the PT connections. Figure 2(c) shows the theoretical cyclic M-θ behavior of the PT connection. After decompression of the PT connection (Point 1 in Figure 2(c)), gap opens and the behavior becomes nonlinear elastic with rotational stiffness S_1. At point 2, the upper WHPs yield and M continues to increase with slope S_2. At point 3, the lower WHPs yield and M continues to increase with slope S_3. When loading is reversed, the connection begins to unload until the gap closes. Equations to calculate S_1 to S_3 and θ_1 to θ_3 are provided in [22].

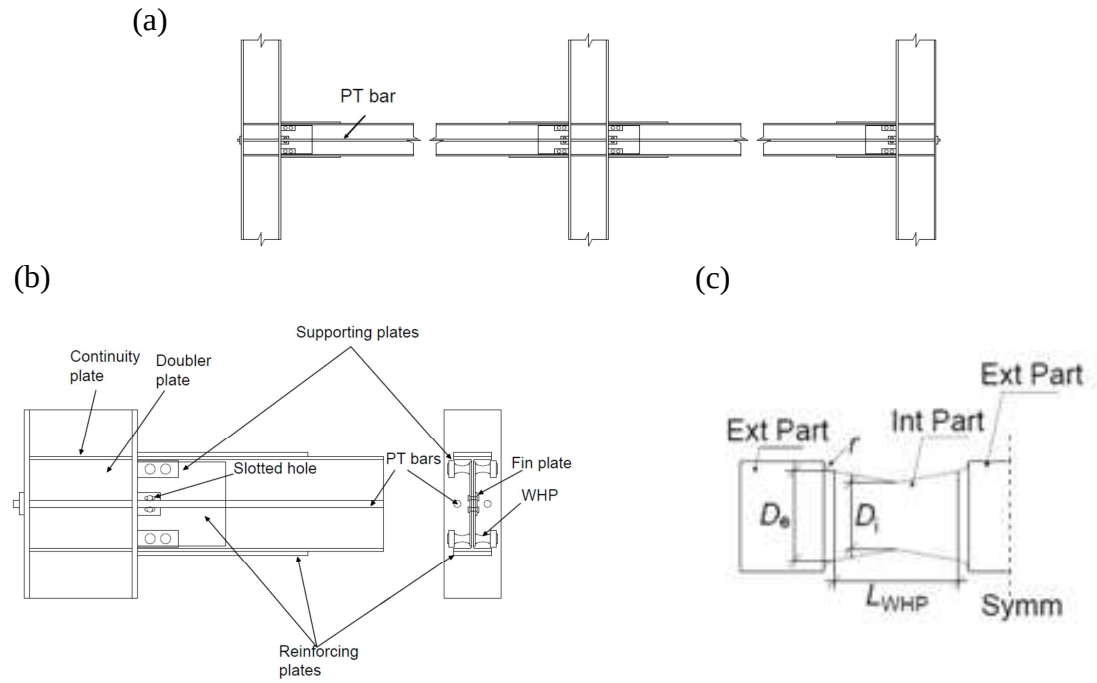

Figure 1. (a) SC-MRF; (b) exterior PT connection with WHPs; and (c) half WHP geometry.

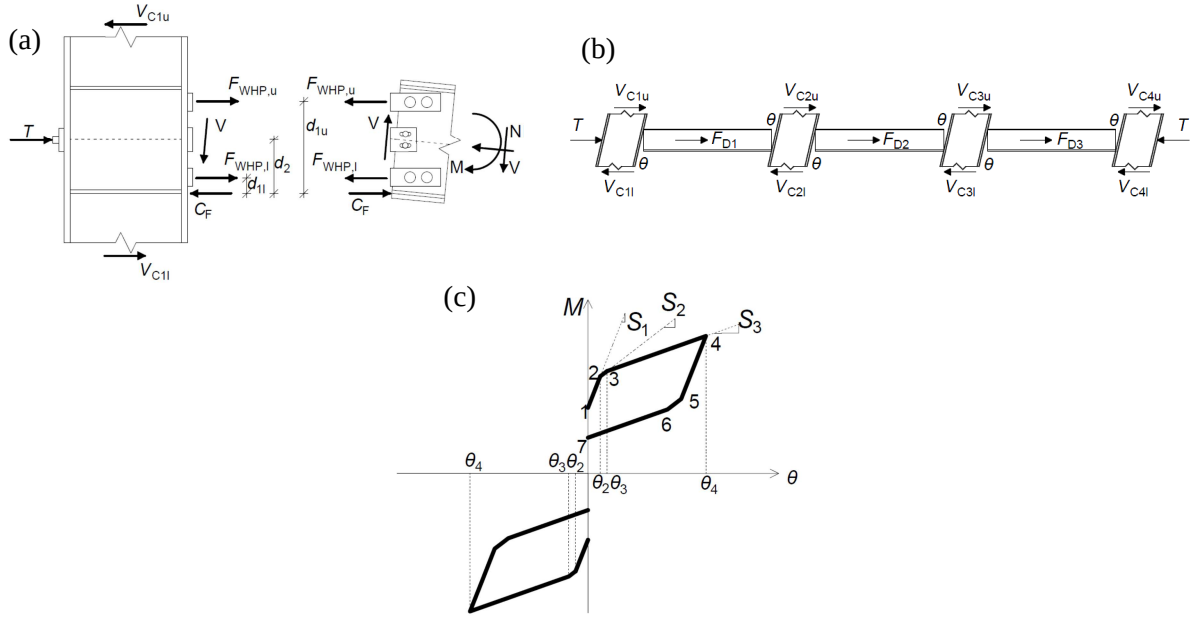

Figure 2. (a) Free body diagram of an external PT connection; (b) SC-MRF expansion and horizontal forces equilibrium; and (c) theoretical cyclic *M-θ* behavior of the PT connection.

3. ECONOMIC SEISMIC LOSS ESTIMATION FRAMEWORK

3.1. Loss estimation framework

According to FEMA P-58 [29], the seismic losses for a building are split into: (a) structural loss due to damage in load-carrying structural members; (b) non-structural loss due to damage in non-load carrying components such as partitions, piping systems, etc.; and (c)

building contents loss. These losses are assessed using detailed component fragility functions, i.e., functions of relevant engineering demand parameters (EDPs), such as the peak story drift ($\theta_{s,max}$) or the peak floor acceleration (PFA) occurred during an earthquake, that determine the probability of violating a certain damage state (DS). Thus, for a given value of the chosen seismic intensity measure (IM), each component is assigned with the corresponding probability of being in any DS, which is then associated with a probabilistic cost function. This function defines the cumulative distribution of the repair cost of the component for the given DS. Summing up all component costs over the entire building yields the total economic seismic loss (see Section 3.4 for more details).

3.2. Probability of collapse and probability of demolition

The probability of collapse can be explicitly incorporated in the loss estimation framework following the methodology in [26], i.e. collapse is assumed to cause instant loss of the entire building and its contents. The probability of demolition can be also explicitly incorporated following the methodology in [27], i.e. by recognizing that the building will be demolished when a critical value of the maximum residual story drift between all stories ($\theta_{s,res}$) is exceeded. For example, McCormick et al. [31] concluded that in Japan it is generally less expensive to rebuild a structure than to repair it when $\theta_{s,res}$ is higher than 0.5%. In this work, the probability of having to demolish the structure conditioned on $\theta_{s,res}$, $P(D|\theta_{s,res})$, is assumed to follow a lognormal distribution with log-standard deviation (standard deviation of the logarithm of the data) equal to 0.3 [27] and a median value equal to 0.5%, 1.0% and 1.5% to allow a parametric study to be conducted.

3.3. Vulnerability functions

The mean annual frequency (MAF) of exceeding values of a decision variable (DV), such as the repair cost or the loss ratio (i.e. repair cost over the building replacement cost), is estimated as [24]:

$$\lambda_{DV}(DV \geq dv) = \int_{IM}\int_{DM}\int_{EDP} G(dv|DM)\left|dG(DM|EDP)\right|\left|dG(EDP|IM)\right|\left|\frac{d\lambda(IM)}{dIM}\right| dIM \qquad (1)$$

where $\lambda_{DV}(DV \geq dv)$ is the MAF of exceeding a loss level *dv* for the given site and building. *G(dv|DM)* is the probability of exceedance of *dv* given a damage measure DM. This continuous DM was employed by Cornell and Krawinkler [24] for theoretical simplicity and it is typically discretized in practice into two or more discrete damage states (DSs) per component to simplify the assignment of associated repair costs. Thus *G*(*DM*|*EDP*), i.e., the probability of exceedance of DM given an EDP, becomes *G*(*DS*|*EDP*), the familiar component fragility function. Finally, *G*(*EDP*|*IM*) is the probability of exceedance of EDP given an IM and λ(*IM*) is the MAF of exceedance of the IM.

In this work, only a part of Equation (1) is used to assess the performance of a building in an objective manner that does not depend on the site, i.e. using only the integrals of loss over EDP and DM (or DS) without the final convolution with λ(*IM*). The result is known as vulnerability function, formally written as:

$$G(dv|IM) = \int_{DM}\int_{EDP} G(dv|DM)|dG(DM|EDP)||dG(EDP|IM)| \qquad (2)$$

Vulnerability functions essentially represent entire distributions of the building loss at each level of the IM. Thus, they can be visualized as continuous curves of any desired distribution statistic given the IM, such as their 16%, 50% and 84% fractile values. Monte Carlo

Simulation (MCS) is used to evaluate the integrals in Equation (2). The MCS procedure involves seven steps (see Section 3.4) and simulates all random variables in Equation (2) (i.e. DV, EDP, DS) to finally compute DV for a wide range of IMs.

3.4. Steps of MCS procedure

Step (1): EDPs prediction. Incremental Dynamic Analysis (IDA) is conducted up to global collapse for a large enough suite of ground motions (44 used in this study), while appropriate interpolation [32] of the analysis results is employed to extract the distribution of the EDPs ($\theta_{s,max}$, PFA and $\theta_{s,res}$) at any level of the IM. The spectral acceleration at the fundamental period of vibration, $S_a(T_1)$, is chosen as IM following FEMA P-58 [29] guidelines. As no scaling limit is employed, nor are the records carefully selected for a given site and intensity level, this approach may be questionable for high levels of intensity, since sufficiency is not assured [33]. Still, this is only an issue when convolution with seismic hazard is attempted (Equation (1)). When using $S_a(T_1)$ solely for comparing the response or vulnerability of buildings with close periods, similar levels of bias will creep in, thus cancelling each other out when taking ratios, as attested, for example, by the spectral-shape correction formula of FEMA P695. Thus, although the absolute values of loss estimated may become conservative at high IM levels, their relevant sizes will remain valid for comparison.

Step (2): Estimate the total replacement cost of the building. The distribution of the replacement cost of the building itself, considering only structural and non-structural components, is estimated using data for new steel construction from [34]. This is augmented by the distribution of the replacement cost for the building contents, as obtained from the corresponding content repair cost functions at their most severe DS [29], indicative of replacement. To combine them, Monte Carlo simulation is employed using uncorrelated stratified sampling. Since we are not interested in the extreme values, but mainly in the first few moments of the uncertain cost, the efficiency of stratified sampling [35] allows us to use only $N = 40$ samples from each constituent distribution to accurately capture the distribution of the total building replacement cost (cost replacement new).

Step (3): Three-dimensional (3D) table 'C'. A 3D table 'C' is created. The number of rows of the table is equal to the IM values (60 $S_a(T_1)$ values from 0 to 4.0g) considered in the loss estimation framework. The number of columns is equal to the number of ground motions (N_{rec}) used to conduct the IDA in Step (1) ($N_{rec} = 44$ in this study), and the third dimension is equal to N, the number of cost samples per distribution. The following steps describe how table 'C' is filled with cost values.

Step (4): Incorporate the probability of collapse. If collapse has occurred for the i^{th} value of IM and the j^{th} ground motion, the $C(i, j, 1{:}N)$ cells are filled by randomly permuting the N total building replacement cost values from Step (2).

Step (5): Incorporate the probability of demolition given no collapse. $\theta_{s,res}$ is obtained for the i^{th} value of IM and the j^{th} ground motion to allow calculation of $P(D|\theta_{s,res})$. If collapse has not already occurred (step 4), N_{dem} (where $N_{dem} = P(D|\theta_{s,res}) \cdot N$) out of the N cells $C(i, j, 1{:}N)$ are randomly filled by using stratified sampling on the total building replacement cost distribution.

Step (6): Estimate the total repair cost of the building given no collapse or demolition. A number of DSs and corresponding fragility curves are defined for each structural, non-structural and content component of the building using data available in FEMA P-58 [29]. For a specific value of an EDP (i.e. $EDP_{i,j}$) corresponding to the i^{th} value of IM and the j^{th} ground motion, the component fragility curve defines the probability $G(DS|EDP_{i,j})$ that the component will experience damage equal or higher than that associated with a specific DS (see Figures 3(a) and 3(b)). Subtracting these probabilities for two sequential DSs provides

the probability $\Delta G(DS|EDP_{i,j})$ of the component to experience damage equal to that associated with a DS (see Figure 3(c)). This probability is multiplied by (N-N_{dem}) to calculate the number of repair cost values (out of N) associated with the DS. Repair cost values are obtained from the cost function of the specific DS and component. Repeating this procedure for all DSs results in N-N_{dem} repair cost values for the component. Repair costs for all components are calculated using the aforementioned procedure and are added to provide the total repair cost values used to fill the remaining N-N_{dem} empty cells of the $C(i, j, 1{:}N)$ matrix, respecting the desired correlation structure. Any of these total repair cost values should be lower than randomly drawn samples of the total building replacement cost, otherwise the former is replaced with the latter on a case-by-case basis.

Step (7): Quantile cost values at each IM. For all $N \cdot N_{rec}$ cost values at the same IM level, quantile values at 16%, 50% and 84% (or any desired distribution statistic) are estimated and plotted.

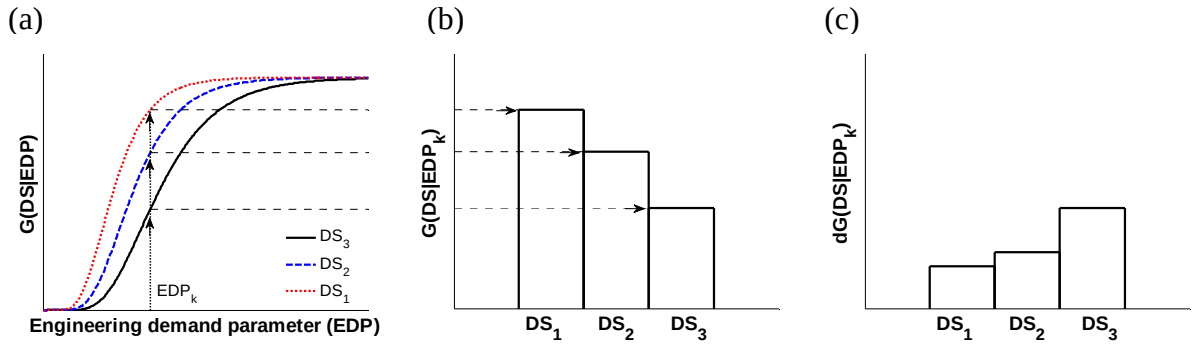

Figure 3. Probability of a component to experience damage corresponding to a DS for a specific value of EDP [28].

4. PROTOTYPE BUILDING AND DESIGN OF THE SEISMIC-RESISTANT FRAMES

Figure 4(a) shows the plan view of a 5-story, 5-bay by 3-bay prototype steel building having two identical perimeter seismic-resistant frames in the 'x' plan direction. The study focuses on one perimeter seismic-resistant frame. This frame is designed as conventional MRF, MRF with viscous dampers, SC-MRF, or SC-MRF with viscous dampers using existing practical seismic design procedures [14-15, 22]. All these designs have the same cross sections. Viscous dampers are installed in the interior gravity frames (with pinned beam-column connections and pinned column bases) that are coupled with the perimeter seismic-resistant frame through the floor diaphragm as shown in Figure 4(b). Inserting dampers in the gravity frames (instead of in the seismic-resistant frames) essentially decouples the extensive design checks of the seismic-resistant frame from the out-of-phase (velocity-dependent) peak damper forces. It is noted that the estimated peak story drifts of the building with viscous dampers do not depend on the position of the viscous dampers (i.e. in gravity frames or in seismic-resistant frames) as the latter does not affect the value of the supplemental viscous damping ratio. The building has ductile non-structural elements, and so, $\theta_{s,max}$ should be lower than 0.75% under the frequently occurring earthquake (FOE) according to EC8 [36]. The DBE is expressed by the Type 1 elastic response spectrum of EC8 with peak ground acceleration equal to 0.35g and ground type B. The FOE has intensity of 40% (reduction factor v=0.4 in EC8) the intensity of the DBE. The maximum considered earthquake (MCE) is taken to have an intensity of 150% the DBE. The model used for the design is based on the

centerline dimensions of the seismic-resistant frame without accounting for the finite panel zone dimensions. The steel yield strength is equal to 355 MPa for the columns, 275 MPa for beams, 930 MPa for PT bars, 235 MPa for the WHPs and 275 MPa for the beam reinforcing plates. Nonlinear viscous dampers are designed with a horizontal configuration (as shown in Figure 4(b)) and a velocity exponent equal to 0.5 to achieve a total damping ratio equal to 20% at the fundamental period of vibration, which is equal to T_1=1.27s. The supplemental equivalent damping ratio at the fundamental mode of vibration is calculated according to [37]. The SC-MRF with dampers and the MRF with dampers have the same total damping ratio. The inherent damping of all frames is 3%. The estimated $\theta_{s,max}$ along all stories under the DBE is equal to 1.2% and 1.8% for the frames with and without viscous dampers, respectively. Design data of the frames are given in Table I.

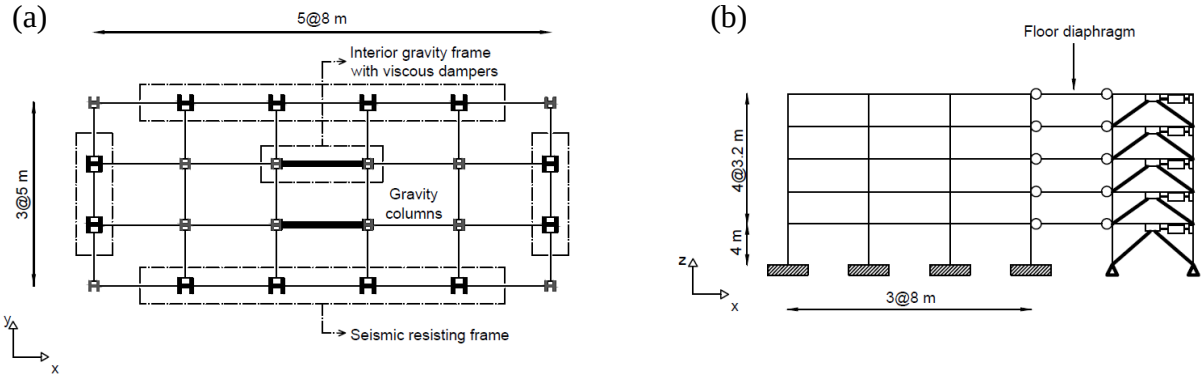

Figure 4. (a) Plan and (b) elevation view of the prototype building.

Table I. Design data of the steel MRF, SC-MRF and viscous dampers.

Story	cross sections		PT connections characteristics							Viscous dampers
			PT force	PT bar diameter	WHP ext. diameter	WHP int. diameter	WHP length	Reinf. plate length	Reinf. plate thickness	
	Beam	Column	T_0 (kN)	d_{PT} (mm)	D_e (mm)	D_i (mm)	L_{whp} (mm)	L_{rp} (mm)	t_{rp} (mm)	c (kN·(s./m)$^{0.5}$)
1	IPE550	HEB650	1087	50	43	33	70	1392	35	2139
2	IPE600	HEB650	1256	60	46	36	70	1660	46	1641
3	IPE550	HEB650	1087	48	43	33	70	1416	35	1416
4	IPE500	HEB600	941	38	41	30	70	1092	26	1102
5	IPE500	HEB600	941	36	39	28	70	743	22	810

It is assumed that the prototype building includes the structural components, non-structural components and contents listed in Table II. Table II lists the type of component, the associated FEMA P-58 identification (ID), the component units that the building includes per story, and the associated EDP used to assess the component DS. Table III lists the components and total buildings costs.

Market research and engineering judgment are used to determine fragility and cost functions for the PT connections, which are not provided by FEMA P-58. The DSs in the PT connections are associated with the replacement of WHPs and the plastic hinge rotation, θ_p, at the end of the beam flange reinforcing plate. θ_p is associated to $\theta_{s,max}$ on the basis of pushover analysis. Replacement of WHPs corresponds to only one DS associated with $\theta_{s,max}$ equal to 1.8% as WHPs have superior cyclic ductility and fracture capacity [30] and there is no need for replacement at lower drifts. The cost functions related to θ_p at the end of the beam flange reinforcing plate were determined using mean and dispersion values from conventional welded moment resisting connections. The labor and material cost of the WHPs, which is

negligible compared to the cost of other building components, has been used to determine the cost function related to WHPs replacement. The contents cost functions have been developed based on USA market prices. The cost of the dampers is based on their stroke and force capacities, and results in a 2% increase of the building cost.

Table II. Prototype building components per story.

MRF components	FEMA P-58 (ID)	SC-MRF components	units	EDP
Steel column base plate	B1031.011b	B1031.011b	8	$\theta_{s,max}$
Post-Northridge welded steel moment connection, beam one side	B1035.021 / None	PT connection, beam one side	4	$\theta_{s,max}$
Post-Northridge welded steel moment connection, beams both sides	B1035.031 / None	PT connection, beams both sides	4	$\theta_{s,max}$
Bolted shear tab gravity connections	B1031.001	B1031.001	28	$\theta_{s,max}$
Curtain walls	B2022.001	B2022.001	54	$\theta_{s,max}$
Suspended ceiling	C3032.003a	C3032.003a	26	PFA
Cold water piping	D2021.011a	D2021.011a	1	PFA
Hot water piping	D2022.012b	D2022.012b	1	PFA
HVAC	D3041.001a	D3041.001a	3	PFA
Modular office work stations	E2022.001	E2022.001	90	PFA
Unsecured fragile objects on shelves	E2022.010	E2022.010	90	PFA
Electronic equipment on wall	E2022.021	E2022.021	1	PFA
Desktop electronics	E2022.022	E2022.022	90	PFA
Book case	E2022.102a	E2022.102a	90	PFA

Table III. Components and total building costs ($\$\cdot 10^6$)

	Component cost				
	MRF	SC-MRF	Gravity frames	Braces and dampers	Non-structural elements
Cost	2.586	2.609	1.522	0.060	1.473
	Total building cost				
	MRF	MRF with dampers	SC-MRF	SC-MRF with dampers	
Cost	5.581	5.641	5.604	5.664	

5. MODELS FOR NONLINEAR ANALYSES

Models for the SC-MRFs are developed in OpenSees [38] as shown in Figure 5. The columns and the reinforced lengths of the beams are modelled as nonlinear force-based beam-column fiber elements with bilinear elastoplastic stress-strain behavior. The assumption of stable hysteresis for the columns is justified because heavy columns with webs and flanges of low slenderness do not show cyclic deterioration even under large drifts (e.g. 9%) [39]. As it shown in Section 6, all frames are close to global collapse for drifts of 9-10%, and therefore, an attempt to model deterioration in columns for drifts higher than 9% would not change the

results of this study. The unreinforced lengths of the beams are modelled using force-based beam-column fiber elements with end hinges [40]. The model in [41] is used for the stress-strain cyclic behavior of the fibers to capture stiffness and strength deterioration due to beam local buckling just after the end of the beam flange reinforcing plates. This modeling approach results in smooth hysteretic curves for flexural members similar to that observed in experiments [42]. Panel zones are modelled using the Krawinkler model [43]. To account for P-Δ effects, the gravity columns associated with the SC-MRFs are modelled as lean-on columns. Diaphragm action is modelled with truss elements connecting the lean-on columns nodes to nodes defined along the length of the beams at the points where secondary beams are placed. These trusses have stiffness of 100 times the axial beam stiffness. The dampers are modelled with zero length viscous elements, while their supporting braces are modelled with elastic braces, as they are strong enough to avoid buckling. In the analytical model, the damper limit states caused by their stroke limit are not considered, i.e. it is assumed that dampers will be manufactured with enough stroke to avoid reaching their limit states even under very large story drifts.

A simplified model for the PT connections with WHPs has been adopted where the M-θ behavior of the PT connection is simulated by inserting 2 parallel rotational springs at the beams ends (see Figure 5). These rotational springs simulate the contribution of the WHPs and the PT bars on the overall rotational behavior of the PT connection. The accuracy of this simplified model has been evaluated against the detailed model in [22], which is based on contact and hysteretic springs at the beam-column interface. Figure 6(a) compares the base shear coefficient (V/W; V: base shear and W: seismic weight) versus roof drift (θ_r) behaviors from nonlinear monotonic static (pushover) analysis, while Figure 6(b) compares the V/W-θ_r behaviors from nonlinear cyclic static (push-pull) analysis of the SC-MRF using either the simplified or the detailed PT connection model.

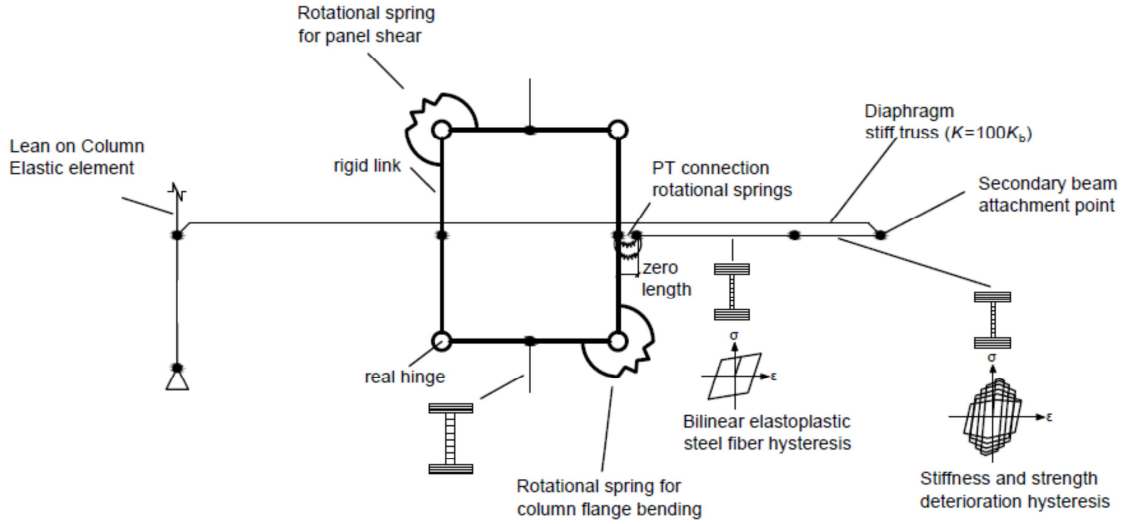

Figure 5. Simplified model for an exterior PT connection and the associated beams and columns.

The connections of the conventional MRF are assumed to be rigid and have full strength, while beams are modeled as elastic elements with zero length rotational springs at their ends that exhibit strength and stiffness deterioration [41]. Columns and panel zones are modeled as described above for the SC-MRF.

The OpenSees models for the SC-MRF and the conventional MRF include the effect of the panel zone stiffness, and so, result in T_1 values shorter than 1.27 s, which is based on the centerline models used for design. T_1 from the OpenSees models is 0.94 s for the SC-MRF

and 1.18 s for the MRF. A Rayleigh damping matrix was used to model the inherent 3% critical damping at the first two modes of vibration.

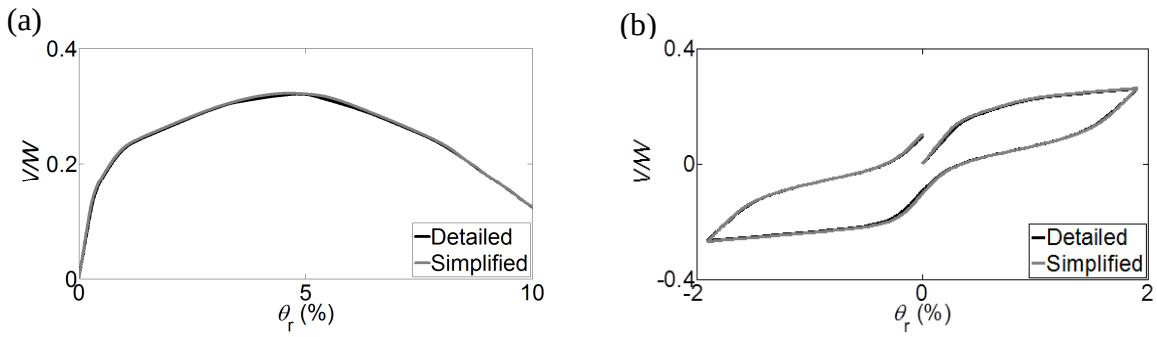

Figure 6. Comparison of the (a) monotonic static (pushover) and the (b) cyclic static (push-pull) behaviors of the SC-MRF using either the simplified or the detailed model in [22] for the PT connections.

6. NONLINEAR STATIC AND INCREMENTAL DYNAMIC ANALYSES

6.1 Nonlinear static analysis

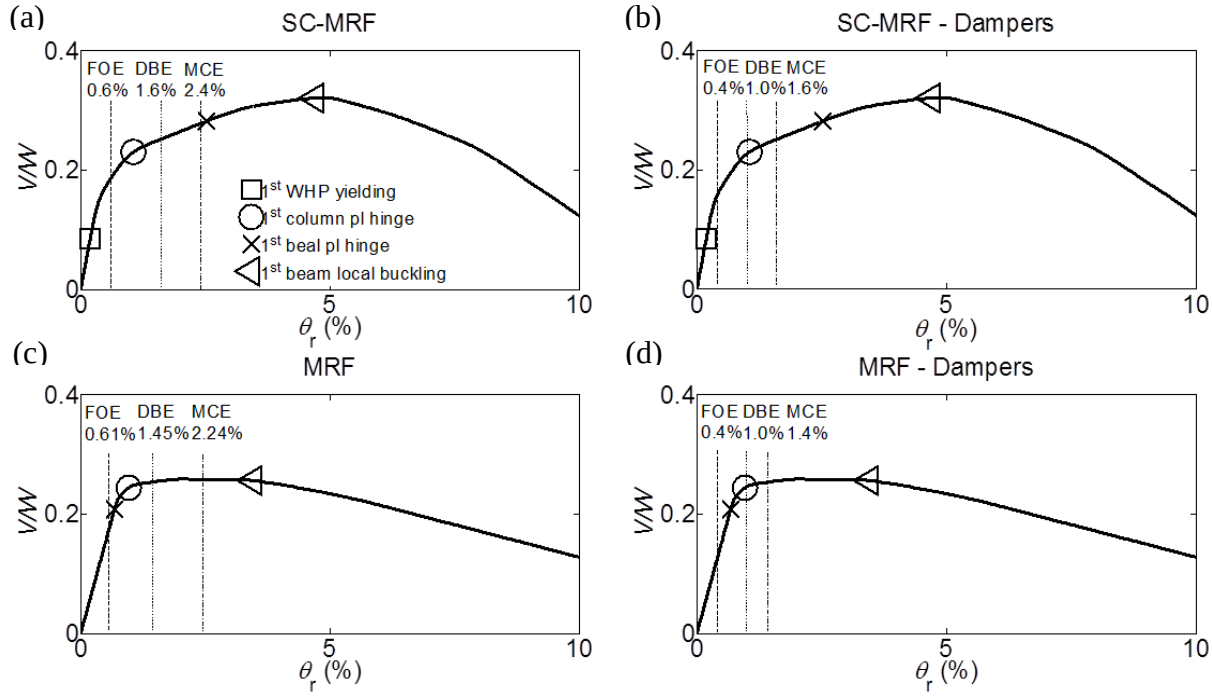

Figure 7. Base shear coefficient - roof drift behavior from nonlinear monotonic (pushover) static analysis.

Figure 7 shows the V/W-θ_r behavior of the SC-MRFs and the conventional MRFs with and without viscous dampers from pushover analysis. Pushover curves are shown along with structural limit states and θ_r estimates under the FOE, DBE and MCE. Figure 7(a) shows the pushover curve of the SC-MRF. WHPs yield at θ_r equal to 0.2%, followed by column plastic hinge at θ_r equal to 1.0%. Plastic hinge at the end of the beam flange reinforcing plate occurs

at θ_r equal to 2.5%. The strength of the SC-MRF continues to increase up to θ_r equal to 4.7%, where beam local buckling occurs and strength deterioration initiates. PT bars do not yield as beam plastic hinge rotations reduce gap opening and PT bar elongation. The peak *V/W* is 0.34. Viscous dampers do not affect the behavior of the SC-MRF under static loading, and so, the SC-MRF with viscous dampers has the same pushover curve (see Figure 7(b)) with the SC-MRF but its performance is better because of the reduction in θ_r estimates under the FOE, DBE and MCE.

Figure 7(c) shows the pushover curve of the conventional MRF. Beam plastic hinge occurs at θ_r equal to 0.7%, followed by column plastic hinge formation at θ_r equal to 1.0% and beam local buckling at θ_r equal to 3.4%. The behavior of the conventional MRF is worse than the behavior of the SC-MRF with the same cross-sections as all structural limit states are reached at lower θ_r. The peak *V/W* is 0.26. The MRF with viscous dampers has the same pushover curve (Figure 7(d)) with the MRF but its performance is better because of the reduction in θ_r estimates under the FOE, DBE and MCE.

6.2 Incremental dynamic analysis and collapse prediction

For all design cases, IDA was performed up to collapse under a set of 22 far-field ground motions pairs (i.e. 44 time histories) used in the FEMA P695 project [44]. For each design case and ground motion, the $S_a(T_1)$ collapse value at which $\theta_{s,max}$ increases without bound was obtained. Each dynamic analysis was extended well beyond the actual earthquake time to allow for damped free vibration decay and accurate $\theta_{s,res}$ calculation. Figure 8 shows the IDA curves of all design cases.

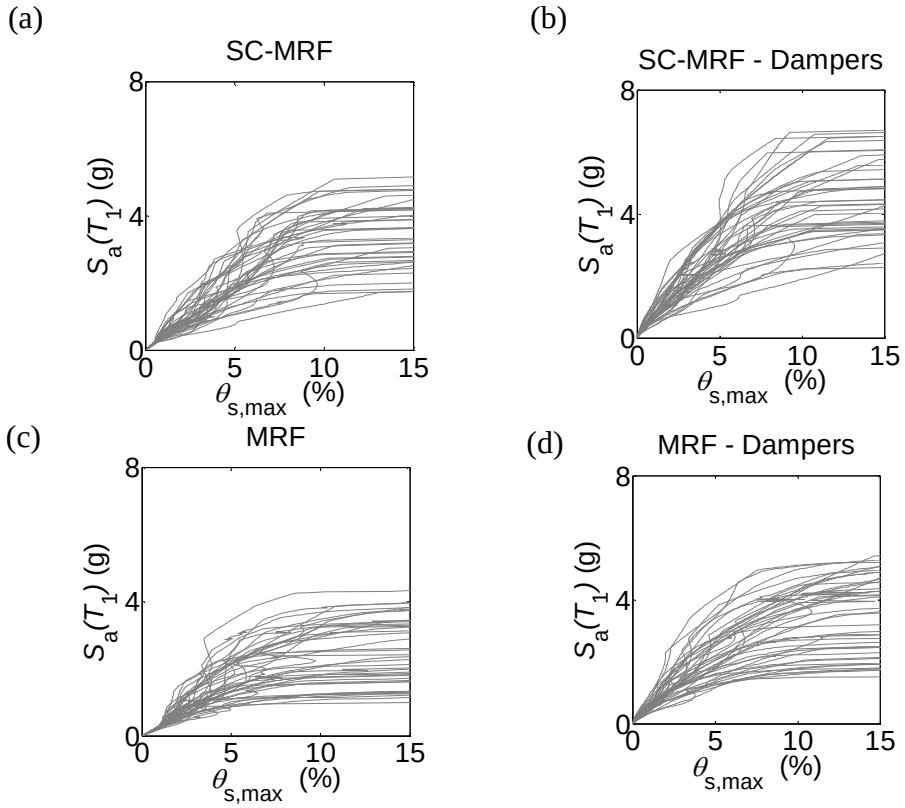

Figure 8. IDA curves of the (a) SC-MRF; (b) SC-MRF with viscous dampers; (c) MRF; and (d) MRF with viscous dampers.

A collapse fragility curve is constructed by fitting a lognormal cumulative distribution function to the $S_a(T_1)$ collapse values as shown in Figure 9(a) for the SC-MRF. Figure 9(b) shows the collapse fragility curves of all design cases, where $S_a(T_1)$ is normalized by $S_{a,MCE}$, i.e. the MCE spectral acceleration at T_1. Beyond just simplifying the discussion to follow, this normalization will also simplify the comparison of structures having (mildly, in this case) different fundamental periods. Thus, the $S_a(T_1)$ at 50% probability of collapse is $5.5 \cdot S_{a,MCE}$ for the SC-MRF with viscous dampers, $5.0 \cdot S_{a,MCE}$ for the MRF with viscous dampers, $4.5 \cdot S_{a,MCE}$ for the SC-MRF and $3.6 \cdot S_{a,MCE}$ for the MRF. The results show that the SC-MRFs have collapse resistance higher than that of the MRFs. It is also evident that supplemental viscous damping significantly improves the collapse resistance of both the MRF and the SC-MRF.

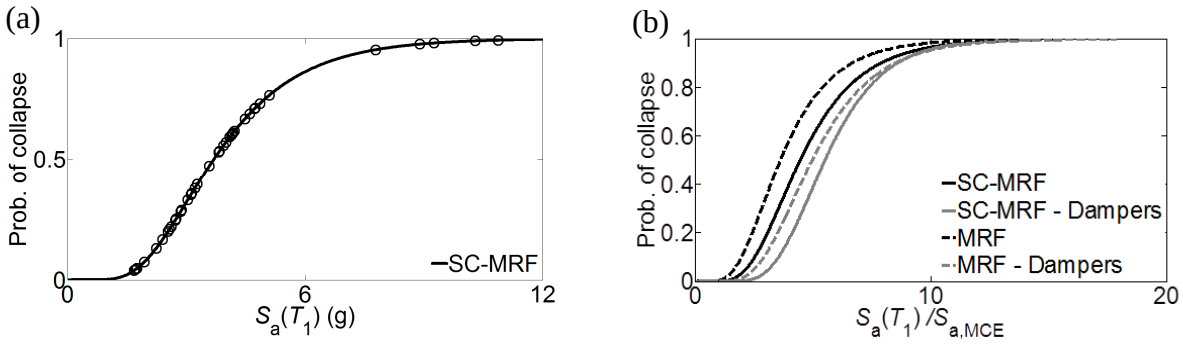

Figure 9. (a) Collapse fragility curve of to SC-MRF fitted to the $S_a(T_1)$ collapse values; (b) collapse fragility curves of all design cases ($S_a(T_1)$ is normalized by $S_{a,MCE}$).

7. ECONOMIC SEISMIC LOSSES

7.1 Vulnerability functions

Figure 10 shows the vulnerability functions of the repair cost and loss ratio at 16%, 50% and 84% probability of exceedance for all frames. These results are obtained for median and lognormal standard deviation values of the $P(D|\theta_{s,res})$ distribution equal to 0.5% [31] and 0.3 [27], respectively. The results clearly show three different regions of loss given IM. First is the low-intensity gradually ascending part that is dominated by non-structural and contents loss plus some early structural damage (mainly due to yielding). Second is the horizontal plateau that appears when demolition (or collapse) starts becoming influential, quickly accelerating losses to reach the total replacement cost. Finally, a near-vertical segment indicates where the building has practically lost all value at high intensities, needing replacement regardless of the specific value of the IM. In all cases, the introduction of dampers clearly pushes the plateau to appear at higher IMs, thus delaying the need for demolition. Post-tensioning seems to have a similar and actually additive beneficial effect. Figure 10 shows that at 50% probability of exceedance, the repair cost of the MRF, the MRF with viscous dampers, the SC-MRF, and the SC-MRF with viscous dampers quickly accelerates after a seismic intensity of 0.9·MCE, 1.2·MCE, 1.9·MCE, and 2.8·MCE, respectively.

Table VI presents repair cost values at 50% probability of exceedance for all design cases and for different seismic intensities. Under the FOE and DBE, the SC-MRF has repair costs similar to those of the MRF. Under the MCE and 2·MCE, the repair costs of the SC-MRF are 92% and 14% less than the repair costs of the MRF, respectively. For higher seismic intensities, the SC-MRF and the MRF have similar repair costs. These results demonstrate

that for a median value of the $P(D|\theta_{s,res})$ distribution equal to 0.5%, post-tensioning is effective in reducing the repair cost for seismic intensities between the DBE and 2·MCE. Under the FOE, DBE and MCE, the MRF with viscous dampers has 100%, 57% and 95% less repair costs than those of the MRF. For seismic intensities equal or higher than the 2·MCE, the MRF and the MRF with viscous dampers have similar repair costs. These results demonstrate that for a median value of the $P(D|\theta_{s,res})$ distribution equal to 0.5%, supplemental viscous damping is effective in reducing the repair cost for seismic intensities lower than 2·MCE. Moreover, Table IV shows that the SC-MRF with viscous dampers has the best performance with repair costs significantly lower than those of the MRF for seismic intensities lower than 3·MCE.

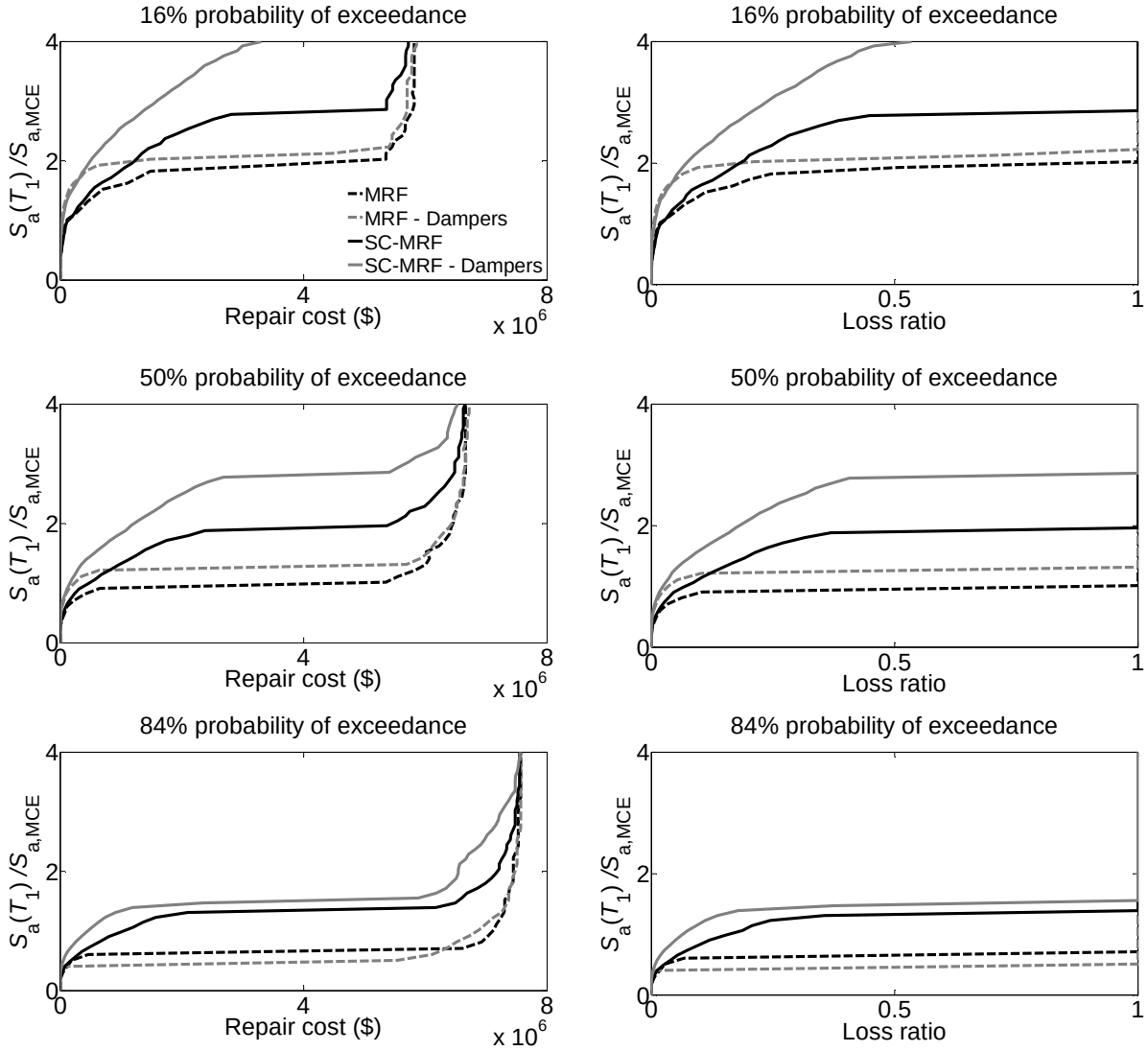

Figure 10. Vulnerability functions of the repair cost and loss ratio at 16%, 50% and 84% probability of exceedance (the $P(D|\theta_{s,res})$ distribution has median value equal to 0.5%).

Table IV. Repair cost (in \$ (10^6)) at 50% probability of exceedance for different seismic intensities (the $P(D|\theta_{s.res})$ distribution has median value equal to 0.5%).

Design cases	FOE	DBE	MCE	2·MCE	3·MCE	4·MCE
MRF	0.01	0.14	5.36	6.46	6.67	6.68
MRF - Dampers	0.00	0.06	0.25	6.46	6.67	6.73
SC-MRF	0.01	0.13	0.45	5.54	6.49	6.66
SC-MRF - Dampers	0.00	0.04	0.16	1.28	5.72	6.54

7.2 Sensitivity of loss estimates to changes in the probability of demolition

To examine the sensitivity of the economic seismic loss to the probability of demolition, additional loss analyses are conducted using median vales of the $P(D|\theta_{s,res})$ distribution equal to 1.0% and 1.5%, while holding the dispersion constant at 0.3. Figures 11 and 12 show vulnerability functions of the repair cost and loss ratio at 50% probability of exceedance for median values of the $P(D|\theta_{s,res})$ equal to 1.0% and 1.5%, respectively. Figure 11 shows that at 50% probability of exceedance, the repair costs of the MRF, the MRF with viscous dampers, the SC-MRF, and the SC-MRF with viscous dampers significantly increase after a seismic intensity of 1.5·MCE, 1.6·MCE, 2.5·MCE, and 3.3·MCE, respectively. The corresponding seismic intensities in Figure 12 are equal to 1.7·MCE, 1.9·MCE, 3.0·MCE, and 3.7·MCE, respectively.

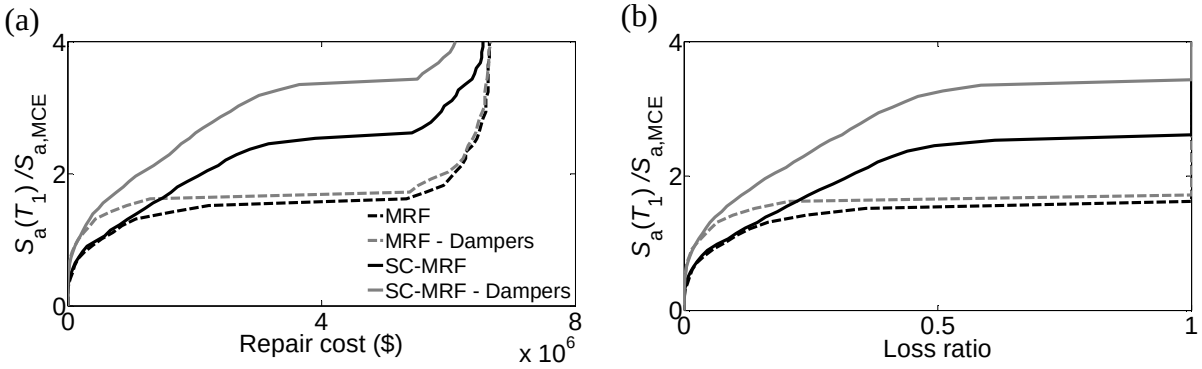

Figure 11. Vulnerability functions of the repair cost and loss ratio at 50% probability of exceedance (the $P(D|\theta_{s.res})$ distribution has median value equal to 1.0%).

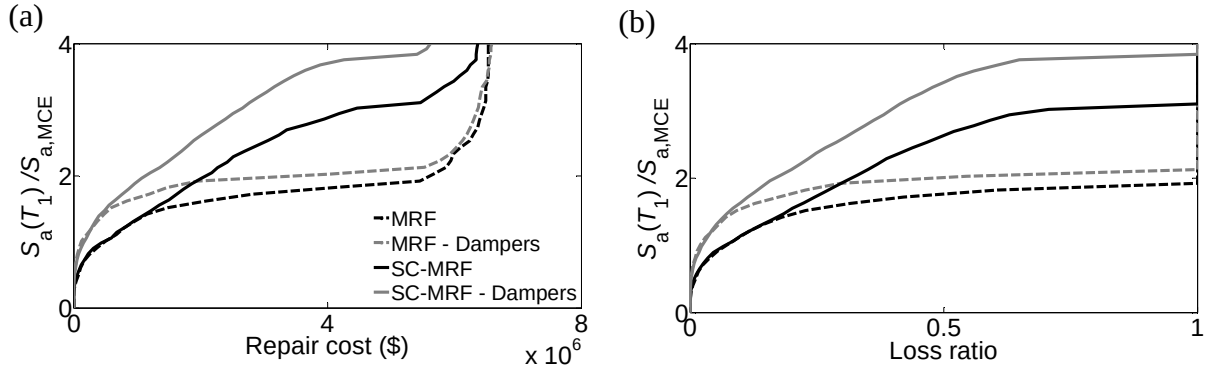

Figure 12. Vulnerability functions of the repair cost and loss ratio at 50% probability of exceedance (the $P(D|\theta_{s.res})$ distribution has median value equal to 1.5%).

Table V presents repair cost values at 50% probability of exceedance for all design cases and for a median value of the $P(D|\theta_{s,res})$ distribution equal to 1.0%. Under the FOE, DBE and

MCE, the SC-MRF has similar repair costs with those of the MRF. Under the 2·MCE, the SC-MRF has 64% less repair costs than those of the MRF. For seismic intensities higher than 3·MCE, the SC-MRF and the MRF have similar repair costs. These results demonstrate that for a median value of the $P(D|\theta_{s,res})$ distribution equal to 1.0%, post-tensioning is effective in reducing the repair cost for seismic intensities between the MCE and 3·MCE. Under the FOE, DBE and MCE, the MRF with viscous dampers has 100%, 73% and 67% less repair costs than those of the MRF. For seismic intensities higher than 2·MCE, the MRF with viscous dampers and the MRF have similar repair costs. These results demonstrate that for a median value of the $P(D|\theta_{s,res})$ distribution equal to 1.0%, supplemental viscous damping is effective in reducing the repair cost for seismic intensities lower than 2·MCE. Table V also shows that the SC-MRF with viscous dampers has the best performance with significantly lower repair costs than those of the MRF for seismic intensities lower than 4·MCE.

Table V. Repair cost (in \$ (10^6)) at 50% probability of exceedance for different seismic intensities (the $P(D|\theta_{s,res})$ distribution has median value equal to 1.0%).

Design cases	$S_{a,FOE}$	$S_{a,DBE}$	$S_{a,MCE}$	$2\cdot S_{a,MCE}$	$3\cdot S_{a,MCE}$	$4\cdot S_{a,MCE}$
MRF	0.01	0.15	0.54	6.11	6.59	6.65
MRF - Dampers	0.00	0.04	0.18	6.00	6.57	6.68
SC-MRF	0.01	0.12	0.45	2.20	5.94	6.54
SC-MRF - Dampers	0.00	0.04	0.16	1.22	2.70	6.11

The results in Table VI show that under the FOE, DBE and MCE, the SC-MRF has repair costs similar to those of the MRF. Under the 2·MCE, 3·MCE and 4·MCE, the SC-MRF has 74%, 55% and 12% less repair costs than those of the MRF. These results demonstrate that for a median value of the $P(D|\theta_{s,res})$ distribution equal to 1.5%, post-tensioning is effective in reducing the repair cost for seismic intensities between the MCE and 4·MCE. Under the FOE, DBE, MCE and 2·MCE, the MRF with viscous dampers has 100%, 75%, 75% and 29% less repair costs than those of the MRF. For seismic intensities higher than 3·MCE, the MRF with viscous dampers and the MRF have similar repair costs. These results demonstrate that for a median value of the $P(D|\theta_{s,res})$ distribution equal to 1.5%, supplemental viscous damping is effective in reducing the repair cost for seismic intensities lower than 3·MCE. Table VI also shows that the SC-MRF with viscous dampers has the best performance with significantly lower repair costs than those of the MRF for seismic intensities equal or lower than 4·MCE.

Table VI. Repair cost (in \$ (10^6)) at 50% probability of exceedance for different seismic intensities (the $P(D|\theta_{s,res})$ distribution has median value equal to 1.5%).

Design cases	$S_{a,FOE}$	$S_{a,DBE}$	$S_{a,MCE}$	$2\cdot S_{a,MCE}$	$3\cdot S_{a,MCE}$	$4\cdot S_{a,MCE}$
MRF	0.01	0.16	0.51	5.67	6.46	6.53
MRF - Dampers	0.00	0.04	0.13	4.05	6.38	6.60
SC-MRF	0.01	0.12	0.44	1.50	2.88	5.72
SC-MRF - Dampers	0.00	0.04	0.15	0.66	1.79	3.04

A careful comparison among the results of Tables IV, V, and VI shows that supplemental viscous damping is more effective than post-tensioning in reducing the repair cost for seismic intensities equal or lower than the MCE. The opposite is true for seismic intensities higher than 2·MCE. The effectiveness of post-tensioning increases as the median of the $P(D|\theta_{s,res})$ distribution increases for seismic intensities equal or higher than the 2·MCE. Moreover, the effectiveness of viscous damping is not clearly affected by the median of the $P(D|\theta_{s,res})$

distribution. In addition, the repair cost of the MRF under the MCE is significantly increased with a decrease of the median of the $P(D|\theta_{s,res})$ distribution from 1.0% to 0.5%. It should be highlighted that seismic intensities higher than MCE have a very low probability of occurrence, yet the paper examines such high seismic intensities to identify the intensity level after which the repair cost of the low-damage SC-MRF with viscous dampers quickly accelerates.

8. CONCLUSIONS

The potential of SC-MRFs and viscous dampers to reduce the economic seismic losses in steel buildings has been evaluated. The evaluation is based on a 5-story prototype steel building designed to use different seismic-resistant frames, i.e.: conventional MRFs; MRFs with viscous dampers; SC-MRFs; or SC-MRFs with viscous dampers. These frames were designed according to Eurocode 8, and have the same beam/column cross-sections and similar periods of vibration. The SC-MRF has similar initial stiffness but higher post-yield stiffness and peak base shear coefficient than the conventional MRF. Viscous dampers are designed to achieve a total damping ratio of 20% at the fundamental mode of vibration. The estimated peak story drift under the design earthquake for the frames with and without dampers is 1.2% and 1.8%, respectively. Incremental dynamic analyses have been conducted using models capable of simulating all structural limit states up to collapse. The economic losses are estimated by developing vulnerability functions according to the FEMA P-58 methodology, which considers uncertainties in earthquake ground motion, structural response, and repair costs. Both the probability of sidesway collapse and the probability of demolition due to excessive residual story drifts are taken into account. Moreover, a parametric study on the effect of the assumed residual story drift value beyond which is less expensive to rebuild a structure than to repair has been conducted. In particular, the probability of having to demolish the building conditioned to residual story drift, i.e. $P(D|\theta_{s,res})$, was assumed to follow a lognormal distribution with median values of 0.5%, 1.0% and 1.5%.

Based on the results presented in this paper and given the properties of the steel frames and ground motions as well as the assumptions used in loss analyses, the following conclusions are drawn:

1. The SC-MRF has higher collapse resistance than that of the MRF, while the use of viscous dampers results in higher collapse resistance for both the MRF and the SC-MRF. The 50% probability of collapse is associated with seismic intensities of 5.5·MCE for the SC-MRF with viscous dampers; 5.0·MCE for the MRF with viscous dampers; 4.5·MCE for the SC-MRF; and 3.6·MCE for the MRF.
2. Three distinct regions of loss given IM are identified, i.e. a low-intensity gradually ascending part that is dominated by non-structural and contents loss plus some early structural damage, followed by a horizontal plateau that appears when demolition (or collapse) starts becoming influential, quickly accelerating losses to reach the total replacement cost. Finally, a near-vertical segment shows where the building has practically lost all value, indicating the need for replacement regardless of the specific value of the IM.
3. The repair cost of the conventional MRF under the MCE significantly increases with a decrease of the median value of the $P(D|\theta_{s,res})$ distribution from 1.0% to 0.5%.
4. Viscous dampers are effective in reducing the repair cost for practically all seismic intensities and regardless of the assumed median value of the $P(D|\theta_{s,res})$ distribution.
5. For a median value of the $P(D|\theta_{s,res})$ distribution equal to 0.5%, post-tensioning is effective in reducing the repair cost for seismic intensities higher than the DBE.

6. For median values of the $P(D|\theta_{s,res})$ distribution equal to 1.0% and 1.5%, post-tensioning is effective in reducing the repair cost for seismic intensities higher than the MCE.
7. Supplemental viscous damping is more effective than post-tensioning in reducing the repair cost for seismic intensities equal or lower than the MCE.
8. The SC-MRF with viscous dampers has superior seismic performance for all seismic intensities. For example, under the DBE and MCE and for all the median values of the $P(D|\theta_{s,res})$ distribution, the SC-MRF with viscous dampers achieves repair costs, which are 70% to 100% less than the repair cost of the conventional MRF.

Acknowledgements

Financial support for this work was provided by the Engineering and Physical Sciences Research Council of the United Kingdom; Grant Ref: EP/K006118/1 (Grant awarded to the 3rd author). The 4th author also acknowledges the support of the European Research Executive Agency via Marie Curie grant PCIG09-GA-2011-293855.

REFERENCES

[1] New Zealand 2013 Treasury Budget Speech. Available online: http://www.treasury.govt.nz/ budget/2013/speech/06.htm (accessed on 14 May 2014).
[2] Canterbury Earthquake Recovery Authority. Available online: http://cera.govt.nz/news/2014/ new-program-to-show-progress-of-public-projects-14 may-2014 (accessed on 14 May 2014).
[3] Ricles J, Sause R, Garlock M, Zhao C. Posttensioned seismic-resistant connections for steel frames. *Journal of Structural Engineering* 2001; 127(2): 113-121.
[4] Christopoulos C, Filiatrault A, Uang CM, Folz B. Posttensioned energy dissipating connections for moment-resisting steel frames. *Journal of Structural Engineering* 2002; 128(9): 1111-1120.
[5] Chou CC, Lai YJ. Post-tensioned self-centering moment connections with beam bottom flange energy dissipators. *Journal of Constructional Steel Research* 2009; 65(10-11): 1931-1941.
[6] Chou C-C, Tsai K-C, Yang W-C. Self-centering steel connections with steel bars and a discontinuous composite slab. *Earthquake Engineering and Structural Dynamics* 2009; 38: 403-422.
[7] Vasdravellis G, Karavasilis TL, Uy B. Large-scale experimental validation of steel post-tensioned connections with web hourglass pins. *Journal of Structural Engineering* 2013; 139(6):1033-1042.
[8] Vasdravellis G, Karavasilis TL, Uy B. Finite element models and cyclic behaviour of self-centering post-tensioned connections with web hourglass pins. *Engineering Structures* 2013; 52:1-16.
[9] Dimopoulos A, Karavasilis TL, Vasdravellis G, Uy B. Seismic design, modelling and assessment of self-centering steel frames using post-tensioned connections with web hourglass shape pins. *Bulletin of Earthquake Engineering* 2013; 11:1797–1816.
[10] Rojas P, Ricles JM, Sause R. Seismic performance of post-tensioned steel moment resisting frames with friction devices. *Journal of Structural Engineering* 2004; 131(4): 529-540.
[11] Kim HJ, Christopoulos C. Friction damped posttensioned self-centering steel moment-resisting frames. *Journal of Structural Engineering* 2008; 134(11): 1768-1779.

[12] Tsai KC, Chou CC, Lin CL, Chen PC, Jhang SJ. Seismic self-centering steel beam-to-column moment connections using bolted friction devices. *Earthquake Engineering and Structural Dynamics* 2008; 37: 627-645.
[13] Wolski M, Ricles JM, Sause R. Experimental study of a self-centering beam-column connection with bottom flange friction device. *Journal of Structural Engineering* 2009; 135(5): 479-488.
[14] Garlock M, Sause R, Ricles JM. Behavior and design of posttensioned steel frame systems. *Journal of Structural Engineering* 2007; 133(3): 389-399.
[15] Kim HJ, Christopoulos C. Seismic design procedure and seismic response of post-tensioned self-centering steel frames. *Earthquake Engineering and Structural Dynamics* 2008; 38(3): 355-376.
[16] Karavasilis TL, Sause R, Ricles JM. Seismic design and evaluation of steel MRFs with compressed elastomer dampers. *Earthquake Engineering and Structural Dynamics* 2012; 41(3): 411-429.
[17] Karavasilis TL, Ricles JM, Sause R, Chen C. Experimental evaluation of the seismic performance of steel MRFs with compressed elastomer dampers using large-scale real-time hybrid simulation. *Engineering Structures* 2011; 33(6):1859-1869.
[18] Karavasilis TL, Seo C-Y. Seismic structural and non-structural performance evaluation of highly damped self-centering and conventional systems. *Engineering Structures* 2011; 33: 2248-2258.
[19] Seo C-Y, Karavasilis TL, Ricles JM, Sause R. Seismic performance and probabilistic collapse resistance assessment of steel moment resisting frames with fluid viscous dampers. *Earthquake Engineering and Structural Dynamics* 2014; 43(14): 2135-2154.
[20] Kurama YC. Seismic design of unbonded post-tensioned precast concrete walls with supplementary viscous damping. *ACI Structural Journal* 2000; 97(3): 648–658.
[21] Kam WY, Pampanin S, Palermo A, Car AJ. Self-centering structural systems with combination of hysteretic and viscous energy dissipations. *Earthquake Engineering and Structural Dynamics* 2010; 39(10): 1083-1108.
[22] Tzimas AS, Dimopoulos AI, Karavasilis TL. EC8-based seismic design and assessment of self-centering post-tensioned steel frames with viscous dampers. *Journal of Constructional Steel Research* 2015; 105:60-73.
[23] Porter KA, Kiremidjian AS, LeGrue JS. Assembly-based vulnerability of buildings and its use in performance evaluation. *Earthquake Spectra* 2001; 17(2):291-312.
[24] Cornell CA, Krawinkler H. Progress and challenges in seismic performance assessment. *PEER Center News* 2000; 3(2):1–4.
[25] Porter, KA, Beck, JL, Shaikhutdinov, RV. Sensitivity of building loss estimates to major uncertain variables. *Earthquake Spectra* 2002; 18 (4): 719-743.
[26] Aslani H, Miranda E. *Probabilistic earthquake loss estimation and loss disaggregation in buildings*, Report No. 157, John A. Blume Earthquake Engineering Research Center, Stanford, CA, 2005.
[27] Ramirez CM, Miranda E. Significance of residual drifts in building earthquake loss estimation. *Earthquake Engineering and Structural Dynamics* 2012; 41:1477-1493.
[28] Gunay S, Mosalam KM. PEER Performance-Based Earthquake Engineering Methodology, Revisited. *Journal of Earthquake Engineering* 2013; 17:829-858.
[29] FEMA P58. Seismic Performance Assessment of Buildings. ATC. Applied Technology Council. CA. USA; 2012.
[30] Vasdravellis G, Karavasilis TL, Uy B. Design rules, experimental evaluation, and fracture models for high-strength and stainless steel hourglass shape energy dissipation devices. *Journal of Structural Engineering* 2015; 140(11):04014087

[31] McCormick J, Aburano H, Ikenaga M, Nakashima M. Permissible residual deformation levels for building structures considering both safety and human elements. *Proc. 14th world conference in Earthquake Engineering*, Seismological Press of China, Paper ID 05-06-0071, Beijing, 2008.
[32] Vamvatsikos D, Cornell CA. Incremental dynamic analysis. *Earthquake Engineering and Structural Dynamics* 2002; 31(3): 491-514.
[33] Luco N, Bazzurro P. Does amplitude scaling of ground motion records result in biased nonlinear structural drift responses? *Earthquake Engineering and Structural Dynamics* 2007; 36(13): 1813-1835.
[34] www.SteelConstruction.info
[35] McKay MD, Beckman RJ, Conover WJ. A comparison of three methods for selecting values of input variables in the analysis of output from a computer code. *Technometrics* 1979; 21(2): 239-245.
[36] EC8. Eurocode 8. Design of structures for earthquake resistance, 2013.
[37] Whittaker AS, Constantinou MC, Ramirez OM, Johnson MW, Chrysostomou CZ. Equivalent lateral force and modal analysis procedures of the 2000 NEHRP Provisions for buildings with damping systems. *Earthquake Spectra* 2003; 19(4):959–80.
[38] OpenSees. Open system for earthquake engineering simulation. Pacific Earthquake Engineering Research Center, University of California at Berkeley, Berkeley, CA, 2013.
[39] Newell J, Uang C-M. Cyclic behavior of steel wide-flange columns subjected to large drift. *Journal of Structural Engineering* 2008; 134:1334-1342.
[40] Scott MH, Fenves GL. Plastic hinge integration methods for force –based beam-column elements. *Journal of Structural Engineering* 2006; 132(2): 244-252.
[41] Lignos DG, Krawinkler H. A database in support of modeling of component deterioration for collapse prediction of steel frame structures. ASCE Structures Congress, SEI institute, Long Beach CA, 2007.
[42] Hamidia M, Filiatrault A, Aref A. Simplified seismic sidesway collapse analysis of frame buildings. *Earthquake engineering and structural dynamics* 2014; 43:429-448.
[43] Krawinkler H. Shear in Beam-Column joints in Seismic Design of Frames. *Engineering Journal* 1978; 15(2) AISC, Chicago, Illinois.
[44] FEMA P695. Quantification of building seismic performance factors. ATC-63 Project. Applied Technology Council. CA. USA, 2008.